Available online at www.sciencedirect.com
SCIENCE DIRECT®
Infrared Physics & Technology 44 (2003) 155–163
INFRARED PHYSICS & TECHNOLOGY
www.elsevier.com/locate/infrared

Detection mechanisms in microstrip dipole antenna-coupled infrared detectors

Iulian Codreanu, Francisco J. Gonzalez, Glenn D. Boreman *

School of Optics/CREOL, University of Central Florida, P.O. Box 162700, Orlando, FL 32816-2700, USA

Received 20 September 2002

Abstract

We compare the detection mechanisms employed in microstrip dipole antenna-coupled infrared detectors. The electrical currents induced along the antenna arms are detected by a rectangular niobium (Nb) microsensor placed at the center of the antenna. The ohmic nature of the Au–Nb contact determines the detection mechanism. Devices with linear contacts between the Au antenna arms and the Nb microsensor exhibit bolometric response. A nonlinear Au–insulator–Nb junction rectifies the induced antenna currents. Devices with nonlinear contacts also exhibit a bolometric response. The devices with nonlinear contacts are $1/f$ noise limited while the devices with linear contacts are Johnson noise limited. The rectification mechanism is 5.3 times faster than the thermal detection. The current–voltage (I–V) characteristic of the devices exhibiting bolometric response is linear, while that of the rectifying devices is cubic. For devices with nonlinear contacts excellent agreement is obtained between the measured detector response and the ratio between the second and the first derivative of the I–V characteristic.

Keywords: IR detector; Infrared antenna; Microstrip dipole; Microbolometer; MIM diode

1. Introduction

Lithographic antenna-coupled infrared detectors were introduced during the mid 1970s [1]. Integrated infrared detectors using dipole antennas [2], bowtie antennas [3], log-periodic antennas [3], spiral antennas [4], microstrip patch antennas [5], and microstrip dipole antennas [6] have been reported. Metal–insulator–metal (MIM) diodes [1,4] and microbolometers [2,3,5,6] integrated with the antennas are used as square-law detectors for the terahertz (THz)-frequency electrical currents induced along the antenna by the incident IR radiation. The advantage of antenna-coupled MIM structures is that the rectification response is substantially faster than the bolometric response, with utility in such applications as frequency mixing measurements.

A bolometer is a thermal detector, sensing a change in its overall temperature. The temperature rise caused by the incident radiation induces a change in the electrical resistance of the bolometer. The temperature coefficient of resistance of a metallic bolometer is positive, while that of a semiconductor bolometer is negative. The change in

* Corresponding author. Tel.: +1-407-823-6815; fax: +1-407-823-6880.
E-mail address: gboreman@mail.ucf.edu (G.D. Boreman).

1350-4495/03/$ - see front matter
doi:10.1016/S1350-4495(02)00224-4

the voltage across a bolometer, ΔV_b is directly proportional to the change in its electrical resistance [7]:

$$\Delta V_b = \frac{V_B R_L \Delta R_b}{(R_L + R_b)^2} \quad (1)$$

where V_B is the bias voltage, R_L is the load resistance from the biasing circuit, and R_b is the resistance of the bolometer.

The MIM diode rectification mechanism can be understood by considering the energy diagram of two similar metallic electrodes separated by an oxide layer of thickness d, as shown in Fig. 1. At equilibrium, the two Fermi levels line up and there is a potential barrier of width d and constant height Φ_0 above the Fermi level E_F. When a potential difference V_b is applied between the electrodes, the Fermi level of the positive-biased electrode moves down by qV_b where q is the unit electronic charge. As a result, the potential barrier between the electrodes has a trapezoidal shape. The height of the potential barrier is a linear function of the distance within the barrier, varying from Φ_0 to Φ_1:

$$\Phi_1 = \Phi_0 - V_b \quad (2)$$

The electrons above the Fermi level in the electrode 1 have a higher probability of tunneling than the electrons from the electrode 2. Therefore, the result of the application of the bias voltage is a net electron flow from electrode 1 to electrode 2.

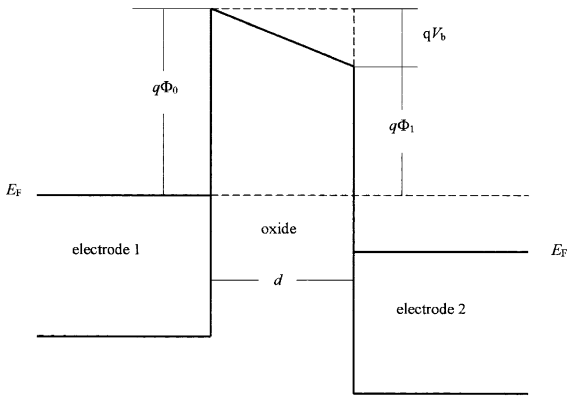

Fig. 1. Energy diagram of two similar electrodes separated by an insulator layer of thickness d.

When the MIM diode is integrated with an antenna the incident IR radiation induces a time dependent "optical voltage" across the barrier, thus modulating the bias voltage. The total bias voltage across the barrier can be expressed as:

$$V(t) = V_b + V_o \cos(\omega t) \quad (3)$$

where V_o is the amplitude of the induced voltage of angular frequency ω in the THz range.

When the induced voltage has the same polarity as the applied voltage, the separation between the Fermi levels is increased and the thickness of the potential barrier is decreased. As a result, the probability of an electron to tunnel through the potential barrier increases and the overall electrical current through the MIM structure increases. Following a similar reasoning, the overall electrical current passing through the diode decreases when the polarity of the induced voltage is opposite to that of the applied voltage. Therefore the MIM diode acts as a rectifier.

To obtain a quantitative relationship between the amplitude of the rectified current, I_r and the amplitude of the induced optical voltage, V_o a Taylor-series expansion of the total current $I(t)$ with respect to the total bias voltage $V(t)$ is performed. The magnitude of the rectified current is related to the amplitude of the induced voltage through [8]:

$$I_r = \frac{1}{4}\left(\frac{d^2 I}{dV^2}\right)_{V_b} V_o^2 \quad (4)$$

The rectified current is proportional to the square of the induced voltage and therefore to the power of the incident radiation. Hence, the MIM diode acts as a square law detector. The proportionality constant is determined by the second derivative of the I–V characteristic of the diode, evaluated at V_b.

Fermi level modulation is not the only mechanism facilitating the tunneling of electrons through the potential barrier. Two other phenomena take place when the IR radiation is incident on the biased junction: (1) photo-assisted tunneling and (2) thermal-assisted tunneling [9]. Photo-assisted tunneling occurs because the electrons in the metals close to the barrier absorb photons and gain $h\omega/2\pi$ extra energy, where h is Planck's constant. In thermal-assisted tunneling, some of the incom-

ing photons are coupled to phonons and the temperature of the metals increases by ΔT. Electrons in the vicinity of the Fermi level will acquire about $k_B \cdot \Delta T$ additional energy, where k_B is Boltzman's constant. The extra energy thus acquired increases the probability of electrons to tunnel through the potential barrier.

We fabricated microstrip dipole antenna-coupled IR detectors that exhibit both bolometric and rectifying detection of the induced antenna currents. Section 2 describes the fabrication of the antenna-coupled detectors using electron-beam lithography. The experimental procedure is presented in Section 3. The two detection mechanisms are investigated in Section 4.

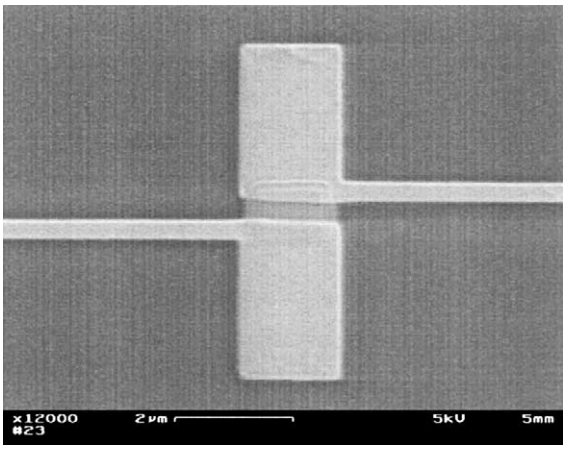

Fig. 2. Electron micrograph of a microstrip dipole antenna-coupled IR detector.

2. Device fabrication

The microstrip dipole antenna-coupled microbolometers were fabricated on 3-in. diameter silicon wafers. A 200-nm thick silicon oxide layer was deposited on the polished side of the wafer by plasma enhanced chemical vapor deposition (PECVD) to provide thermal and electrical insulation between the device and the silicon wafer. A 200-nm thick layer of evaporated gold served as antenna ground plane. The dielectric spacer between the dipole and the ground plane consisted of a 500-nm thick layer of silicon oxide deposited by PECVD. Fig. 2 shows a top view of the integrated sensor. A 100-nm thick layer of gold was electron-beam evaporated on top of a bi-layer of electron-beam resist in which the antenna pattern had been defined. A thin (10 nm) layer of evaporated titanium (Ti) served as adhesion layer between the silicon oxide and gold layers. The excess metal was removed by lift-off. The two antenna arms were nominally 1.8 μm wide and were separated by a 400-nm long gap. The narrow (300 nm) horizontal lines shown in Fig. 2 were deposited simultaneously with the dipole antenna arms, and serve as direct current (dc) leads connecting the antenna to the biasing and read-out circuit. However, the dc leads also collect some IR radiation and thus reduce the overall antenna polarization ratio. To alleviate this problem, the dipole antenna arms were made wider than the dc leads, taking advantage of the fact that a larger-area antenna has a larger radiation collection area. A rectangular ($1.8 \times 1.0\ \mu m^2$) bolometer pattern, defined in an electron-beam resist layer, was aligned with the gap between the two antenna arms. A 100-nm thick layer of Nb was deposited by dc sputtering and the excess metal was lifted off. The electrical resistance of the integrated detectors was about 50 Ω.

3. Experimental setup

Fig. 3 shows the optical train used for the illumination of the integrated detectors. The carbon dioxide (CO_2) laser emits linearly polarized radiation at 10.6 μm. A set of neutral-density filters attenuates the laser beam. The polarizer (P) further reduces the optical power. In conjunction with the half-wave plate (HWP), it controls the polarization of the radiation that eventually reaches the detector. Lenses L1 and L2 form an afocal system used to collimate and expand the beam by a factor of 20. An F/1 aspheric lens (L3) focuses the beam into an almost diffraction-limited spot with a $1/e^2$ radius of 13 μm and an irradiance of about 1000 W/cm^2. The detector under test was biased at 100 mV and placed in the focal plane of the aspheric lens. The mechanical chopper, placed in the focal plane of the first lens, modulated the laser beam at

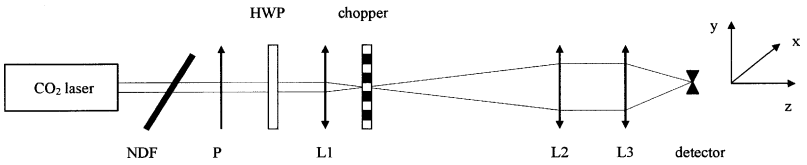

Fig. 3. Schematic of the optical train used to illuminate the detectors.

2.5 kHz and the change in the voltage across the terminals of the detector was recorded using a lock-in amplifier after a $10\times$ preamplification. Both the magnitude and the phase of the detector response were read from the lock-in amplifier.

The device was mounted on a three-axis micropositioner stage. Two computerized Melles-Griot nanomovers controlled the position of the detector in the vertical (x–y) plane. The movement along the beam-propagation direction (z) was controlled manually. To record the spatial response of the detector, a two-dimensional serial scan with a resolution of 1μm was performed by moving the device in the x–y plane.

4. Results and discussion

Fig. 4 shows a typical two-dimensional scan of the spatial response of a microstrip dipole antenna-coupled microbolometer. The response consists of a central peak superimposed onto a pedestal. The incident radiation raises the temperature of the microbolometer through several mechanisms. First, the antenna currents at optical frequencies induced by the incident radiation are dissipated within the bolometer. We refer to the signal generated through this detection mechanism as the *antenna thermal signal*. Second, the radiation absorbed directly into the bolometer and into the substrate in the vicinity of the antenna also raises the temperature of the bolometer. The signal generated through this detection mechanism is referred to as the *substrate thermal signal*. Third, the gold dc leads provide a conduction path for the heat generated within the silicon oxide antenna substrate to the microbolometer. We will refer to the signal generated through this detection mechanism as to the *dc leads thermal signal*. The central peak of the spatial response is generated through the first two mechanisms. The horizontal dc leads (see Fig. 2) are responsible for the generation of the pedestal onto which the central peak is superimposed.

Fig. 5 shows the spatial response of devices fabricated under slightly different conditions. It consists of a central response accompanied by two side lobes of opposite polarity. The electron-beam resist layer used to define the bolometer pattern was selectively exposed with an electron dose of 300 μC/cm^2. The bolometer pattern of the devices whose spatial response is shown in Fig. 4 was de-

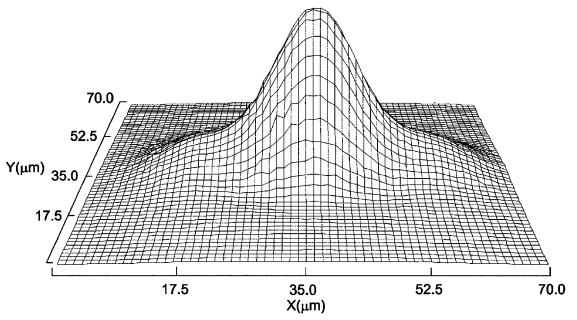

Fig. 4. Two-dimensional scan of the spatial response of an integrated detector with ohmic contacts.

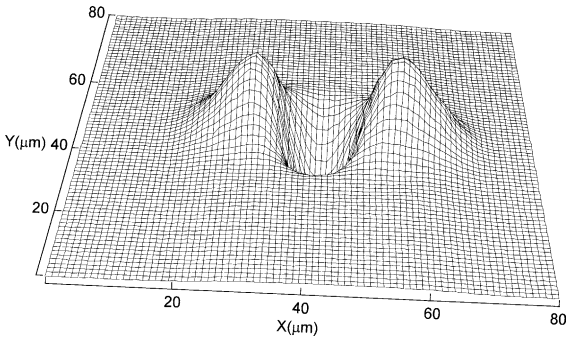

Fig. 5. Two-dimensional scan of the spatial response of an integrated detector with nonlinear contacts.

fined by exposing the resist with a higher dose (500 $\mu C/cm^2$). After exposure, the resist was developed for 60 s in both cases.

Because of the lower exposure dose a thin (tens of angstroms) layer of resist is left on top of the Au antenna arms and is sandwiched between the Nb microsensor and the antenna arms. Fig. 6(a) shows the energy diagram at equilibrium for a Nb microsensor of length L placed on top of two Au antenna arms when a resist layer of thickness d exists between the microsensor and the antenna arms. Gold has a larger work function ($\Phi_{Au} = 5.1$ eV) than niobium ($\Phi_{Nb} = 4.3$ eV) [10]. The energy diagram after the application of a bias voltage V_b is shown in Fig. 6(b). The width of the energy barrier seen by the electrons close to the Fermi level in the first dipole arm is reduced as a result of the application of the bias voltage. Those electrons tunnel from the first dipole arm into the Nb microsensor with higher probability. The bias voltage also increases the tunneling probability of electrons from the Nb microsensor into the second dipole arm. The bias voltage reduces the probability of electrons tunneling from the second dipole arm into the Nb microsensor and from the Nb microsensor into the first dipole arm. Therefore the result of the application of the bias voltage is a net electron flow from the first antenna arm to the second antenna arm, via the Nb microbolometer. The *optical voltage* induced across the two nonlinear contacts and the microsensor by the incident IR radiation modulates the separation between the Fermi levels and thus modifies the tunneling probabilities of the electrons as described in Section 1. The signal generated through this detection mechanism will be referred to as the *rectified signal*. The rectified antenna current dissipates in the Nb microsensor generating an *antenna thermal signal*.

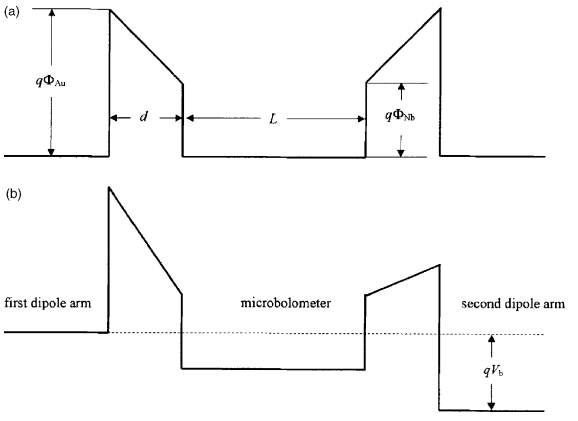

Fig. 6. Energy diagram of a niobium microbolometer of length L placed between two gold electrodes. Two nonlinear contacts are formed at the gold-niobium contacts because of the resist of thickness d.

Three detection mechanisms are present in these devices: (1) the rectification of the induced antenna currents by the nonlinear contacts formed between the Nb microsensor and the antenna arms; (2) the bolometric detection of the rectified antenna currents by the Nb microsensor; and (3) the thermal detection of the radiation directly absorbed into the Nb microsensor and into the antenna substrate. The first two detection mechanisms are dependent on the antenna design because they are based on the induced antenna currents. The third detection mechanism is mainly determined by the size and irradiance of the laser beam used to illuminate the device under test. The second and third detection mechanisms are thermal in nature and occur because of the increase of the overall temperature of the Nb microsensor. The central portion of the detector spatial response shown in Fig. 5 is the result of the competition between the rectification mechanism and the two thermal detection mechanisms. The positive side lobes are thermal in nature and are generated by the heat conducted from the silicon oxide antenna substrate into the microsensor via the dc leads.

Fig. 7 compares the detector response versus the bias voltage of the devices exhibiting only thermal response to that of the devices in which both the rectification and thermal mechanisms are present. We compare only the central portions of the spatial response. The curves follow the sign convention adopted earlier. Devices exhibiting both detection mechanisms have linear response only in the −100 to 100 mV bias voltage range. Within this linear response range the slope of the curve (-1.9×10^{-2} V/V) is steeper than the slope of the devices exhibiting only the thermal detection mechanisms (6.8×10^{-3} V/V). Saturation of the

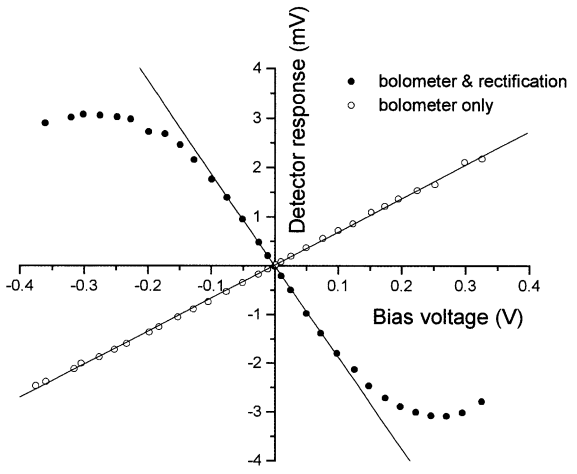

Fig. 7. Detector response versus bias voltage. The polarity of the response of the devices with nonlinear contacts is opposed to that of devices with linear contacts.

detector response starts at about 200 mV. The detector response rolls over for bias voltages in excess of 275 mV. In contrast, the response of the devices exhibiting only thermal response is linear throughout the entire bias voltage range.

Fig. 8 shows the magnitude of the central portion of the detector spatial response as a function of the antenna length for devices exhibiting both rectification and thermal detection. The detectors were biased at 100 mV and illuminated with 10.6-μm wavelength CO_2 laser radiation. As seen in Fig. 7, at 100 mV bias voltage the rectified signal is stronger than the antenna thermal signal. For short antennas the rectification mechanism is dominant over the thermal mechanisms because the antenna length is close to the resonant length and the induced THz currents are strong. As the antenna length increases, the magnitude of the induced THz currents decreases and the substrate thermal signal becomes more important. When the combined thermal signal equals the rectified signal, the detector signal goes through zero. For antennas longer than 4 μm, the detector signal is thermal in nature and almost constant in magnitude. In [6] (Fig. 2) we have shown that the magnitude of the current induced at the center of the microstrip dipole antenna by the CO_2 laser radiation does not change significantly for antenna lengths between 4 and 7 μm. Therefore the two antenna signals are almost constant for this range of antenna lengths. It can be concluded that the substrate thermal signal is independent of the antenna size.

To further investigate the differences between the two detection mechanisms, time constant measurements were performed. A germanium acousto-optic modulator, placed between the polarizer and the HWP, modulated the laser beam up to 10 MHz. Fig. 9 shows the normalized detector response versus modulation frequency for both the central response with negative polarity and for the

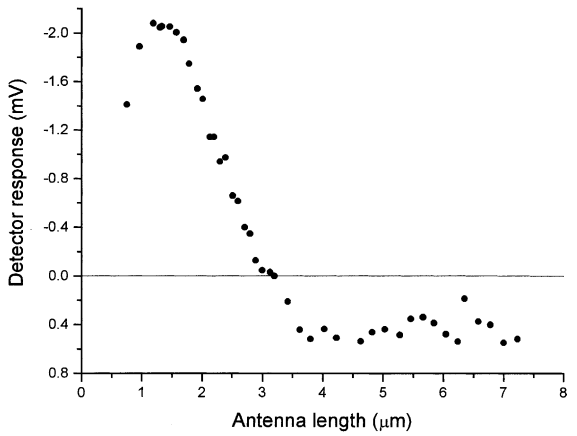

Fig. 8. Detector response versus antenna length for 10.6-μm wavelength incident radiation. The rectification mechanism dominates at short antenna lengths.

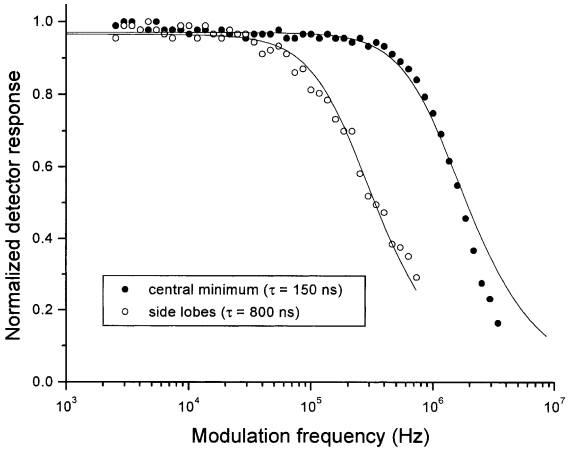

Fig. 9. Normalized detector response versus modulation frequency.

positive side lobes of Fig. 5. The central response is about 5.3 times faster than the response from the dc leads. This was expected because the rectification of the antenna currents by a nonlinear junction is faster than thermal detection.

Fig. 10 compares the noise voltage spectrum at 100 mV bias of devices exhibiting only thermal response to the noise voltage spectrum of devices exhibiting both rectification and thermal response. The noise voltage spectrum was calculated by taking the square root of the difference between the measured noise power spectrum and the instrumental noise power spectrum. The electrical resistance of both types of devices was nominally 50 Ω. In the devices exhibiting both detection mechanisms, the total noise is dominated by the $1/f$ noise at low frequencies and tends towards the Johnson noise level of a 50-Ω resistor at high frequencies. Johnson noise is the sole noise source in devices exhibiting only thermal response. The $1/f$ noise voltage is inversely proportional to the square root of the frequency. The proportionality constant depends on the ohmic nature of the junction between electrodes; a high quality junction generates low $1/f$ noise. This shows that the ohmic quality of the Au–Nb junctions in the rectifying devices is poorer than in the devices showing only thermal response.

Current–voltage (I–V) measurements were performed using a probe station and an HP4145B semiconductor parameter analyzer. Fig. 11 compares the I–V characteristics for devices showing only thermal detection and for devices exhibiting both detection mechanisms. The device exhibiting both detection mechanisms had a 1.8-μm long dipole antenna; in this device the rectification mechanism dominates the thermal detection (see Fig. 8). The I–V characteristic of the bolometric devices is linear while the I–V characteristic of the devices exhibiting both detection mechanisms has a cubic dependence on the bias voltage.

Throughout this work we referred to the change in the bias voltage across the detector induced by the incident IR radiation as the *detector response*. Eq. (4) shows that the rectified current I_r is proportional to the second derivative of the I–V characteristic. The detector response is obtained by multiplying the rectified current by the electrical resistance of the detector:

$$V_{out} = RI_r \tag{5}$$

The electrical resistance of the detector at a given bias voltage is the inverse of the first derivative of the I–V characteristic, evaluated at that particular bias voltage. Therefore, the magnitude of the signal generated by a device exhibiting rectifying detection is directly proportional to the second derivative of the I–V characteristic and inversely

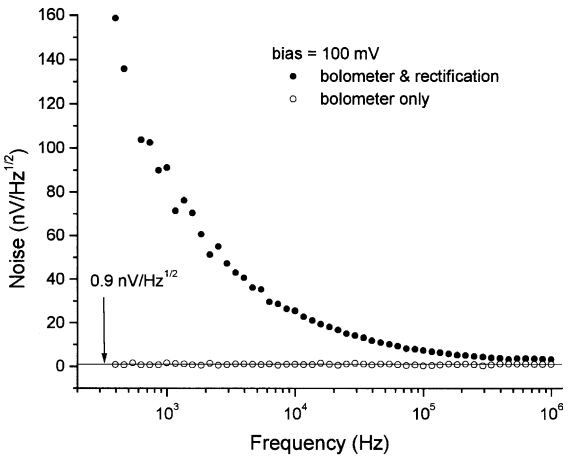

Fig. 10. Noise voltage spectrum at 100 mV bias. Devices with linear contacts are Johnson noise limited while the devices with nonlinear contacts are $1/f$ noise limited.

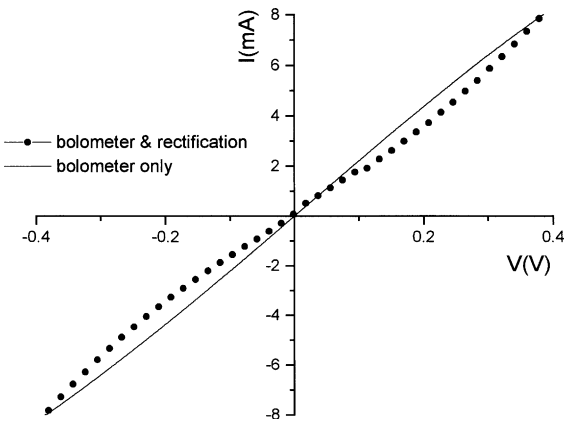

Fig. 11. I–V characteristics. Devices exhibiting bolometric detection have a linear I–V characteristic while the characteristic of the rectifying devices is nonlinear.

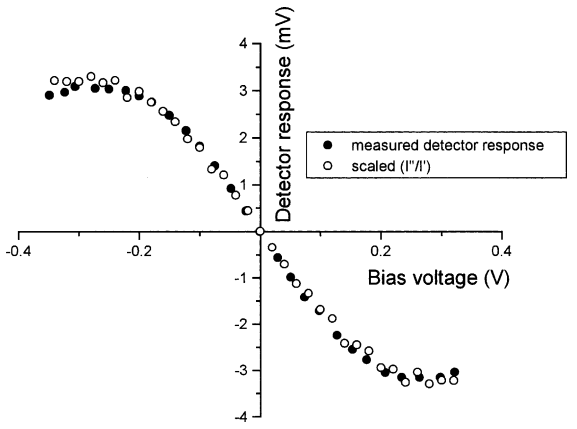

Fig. 12. Detector response versus bias voltage compared to the ratio between the second and the first derivatives of the I–V characteristic for a device exhibiting both detection mechanisms. The antenna length (1.8 μm) was close to the resonant length rendering the rectification mechanism dominant.

proportional to the first derivative of the I–V characteristic:

$$V_{\text{out}}(V_{\text{b}}) \propto \frac{I''(V_{\text{b}})}{I'(V_{\text{b}})} \tag{6}$$

Fig. 12 shows the excellent agreement between the measured detector response and the ratio between the second and the first derivative of the I–V characteristic. The derivatives of the I–V characteristic were obtained from the data shown in Fig. 11.

5. Conclusions

We investigated the detection mechanisms in microstrip dipole antenna-coupled IR detectors. The nature of the detection mechanism depends on the quality of the contact between the Au antenna and the Nb microsensor placed at the center of the antenna. A linear ohmic contact generates a bolometric response, referred to as the antenna thermal signal, because the induced antenna currents dissipate within the microsensor. Another thermal signal, referred to as substrate thermal signal, is generated because of the absorption of the incident IR radiation into the microsensor and into the antenna substrate.

During the fabrication process, a photo-resist residue can be incorporated between the antenna arms and the Nb microsensor leading to nonlinear Au–insulator–Nb contacts. These nonlinear contacts rectify the induced antenna currents. The rectified antenna currents dissipate in the microsensor, leading to an antenna thermal signal. Radiation absorbed into the microsensor and into the antenna substrate leads to the generation of a substrate thermal signal. Because the respective signals have opposite polarity, the rectification mechanism competes against the two thermal mechanisms in devices with nonlinear contacts. In antennas with lengths close to the resonant length the rectification mechanism dominates the two thermal mechanisms. The substrate thermal response is essentially independent of the antenna length. As the antenna length increases the induced electrical current decreases in magnitude and the substrate thermal response becomes the dominant detector signal.

The dc leads used to bias the device provide a conduction path for the heat generated within the antenna substrate towards the Nb microsensor. When the laser beam is incident onto the dc leads both the devices with linear ohmic contacts and the devices with nonlinear contacts generate a response that is thermal in nature.

The rectification mechanism is more than five times faster than the thermal detection mechanism. The $1/f$ noise is dominant in devices incorporating nonlinear contacts while the devices with linear contacts are Johnson noise limited.

Devices exhibiting only bolometric detection have a linear I–V characteristic while the I–V characteristic of devices exhibiting both detection mechanisms is nonlinear. The response of the detectors exhibiting only thermal detection is linear throughout the −400 to 400 mV bias voltage range. Devices with both detection mechanisms exhibit linear response only within the −100 to 100 mV bias voltage range. The response of those devices saturates above 200 mV and rolls over for bias voltages exceeding 275 mV. The measured detector response versus bias voltage for devices with nonlinear contacts is in excellent agreement with the ratio between the second and the first derivative of the I–V characteristic.

Acknowledgements

This material is based upon work supported by NASA under grant number NAG5-10308. This work was performed in part at the Cornell Nanofabrication Facility (a member of the National Nanofabrication Users Network), which is supported by the National Science Foundation under Grant ECS-9731293, Cornell University and industrial affiliates.

References

[1] S.Y. Wang, T. Izawa, T.K. Gustafson, Coupling characteristics of thin-film metal-oxide-metal diodes at 10.6 μm, Appl. Phys. Lett. 27 (1975) 275–279.

[2] C. Fumeaux, M.A. Gritz, I. Codreanu, W.L. Schaich, F.J. Gonzalez, G.D. Boreman, Measurement of the resonant lengths of infrared dipole antennas, Infrared Phys. Technol. 41 (2000) 271–281.

[3] N. Chong, H. Ahmed, Antenna-coupled polycrystalline silicon air-bridge thermal detector for mid-infrared radiation, Appl. Phys. Lett. 71 (1997) 607–1609.

[4] C. fumeaux, G.D. Boreman, W. Herrmann, H. Rothuizen, F.K. Kneubuhl, Polarization response of asymmetric-spiral infrared antennas, Appl. Opt. 36 (1997) 6485–6490.

[5] I. Codreanu, C. Fumeaux, D.F. Spencer, G.D. Boreman, Microstrip antenna-coupled infrared detector, Electron. Lett. 35 (1999) 2166–2167.

[6] I. Codreanu, G.D. Boreman, Infrared microstrip dipole antennas—FDTD predictions versus experiment, Microwave Opt. Technol. Lett. 29 (2001) 381–383.

[7] E.L. Dereniak, G.D. Boreman, Infrared detectors and systems, John Wiley & Sons, New York, 1996.

[8] S.M. Faris, B. Fan, T.K. Gustafson, Electronic tunneling currents at optical frequencies, Appl. Phys. Lett. 27 (1975) 629–631.

[9] M. Heiblum, S. Wang, J.R. Whinnery, T.K. Gustafson, Characteristics of integrated MOM junctions at dc and at optical frequencies, IEEE J. Quantum Electron. 14 (3) (1978) 159–169.

[10] D.R. Lide, H.P.R. Frederiske (Eds.), CRC Handbook of Chemistry and Physics, CRC Press, Boca Raton, 1996.